International Conference on Adaptive Modeling and Simulation
ADMOS 2023
F.Larsson and P.Díez

ON THE DISCRETIZATION OF THE CONTINUOUS ADJOINT TO THE EULER EQUATIONS IN AERODYNAMIC SHAPE OPTIMIZATION

MARINA G. KONTOU, XENOFON S. TROMPOUKIS, VARVARA G. ASOUTI AND KYRIAKOS C. GIANNAKOGLOU

Parallel CFD & Optimization Unit, School of Mechanical Engineering
National Technical University of Athens, Athens, Greece
e-mail: mkontou@mail.ntua.gr, xeftro@gmail.com, vasouti@mail.ntua.gr, kgianna@mail.ntua.gr

Key words: Continuous Adjoint, Discretization Schemes, Aerodynamic Shape Optimization, Euler Equations

Summary. In aerodynamic shape optimization, gradient-based algorithms usually rely on the adjoint method to compute gradients. Working with continuous adjoint offers a clear insight into the adjoint equations and their boundary conditions, but discretization schemes significantly affect the accuracy of gradients. On the other hand, discrete adjoint computes sensitivities consistent with the discretized flow equations, with a higher memory footprint though. This work bridges the gap between the two adjoint variants by proposing consistent discretization schemes (inspired by discrete adjoint) for the continuous adjoint PDEs and their boundary conditions, with a clear physical meaning. The capabilities of the new *Think-Discrete-Do-Continuous* adjoint are demonstrated, for inviscid flows of compressible fluids, in shape optimization in external aerodynamics.

1 INTRODUCTION

In aerodynamic shape optimization, gradient-based methods are attractive since, thanks to the adjoint method, can efficiently compute the extrema of an objective function J, by computing its gradient with respect to (w.r.t.) the design variables. With the (continuous or discrete) adjoint method, the cost of computing the gradient of J is independent of the number of the design variables. The ease of implementation, the insight into the adjoint PDEs and the low memory footprint are the main advantages of continuous adjoint, [1, 2]. On the other hand, discrete adjoint, [3, 4, 5], computes the gradient of the objective/constraint function(s) with max. accuracy, thanks to the consistency of the discretized primal (flow) and adjoint equations. This paper develops discretization schemes for the (continuous) adjoint PDEs which are inspired by, and are consistent with, discrete adjoint. In other words, we combine the advantages of continuous and discrete adjoint into a new *Think-Discrete-Do-Continuous* (*TDDC*) adjoint, with low memory footprint and comprehensible discretization schemes. Here, the development is restricted to inviscid flow models for compressible flows. Due to limitations on the number of pages, we

refrain from presenting the discretization of sensitivity derivatives (SDs). The new *TDDC* adjoint is used for the shape optimization of an airfoil and a wing, both at flow conditions that lead to transonic flows. All runs are carried out using the in-house GPU–accelerated flow simulation and adjoint-based optimization platform PUMA, [7]. PUMA solves the Reynolds-Averaged Navier-Stokes equations for compressible and incompressible fluids (here, the compressible variant, for inviscid flows, is used).

In a similar work, [6], the discrete adjoint fluxes were derived by hand and, through reverse-engineering, discretization schemes for some of the continuous adjoint terms were devised, for incompressible flows solved using the segregated pressure-based algorithm.

2 PRIMAL PROBLEM & ITS DISCRETIZATION

The inviscid flow equations for 3D compressible flows are solved in the form

$$R_n^{MF} = \frac{\partial f_{nk}}{\partial x_k} = 0 \quad , \quad n = 1,..,5, \quad k = 1,...,3 \tag{1}$$

where $f_{nk} = [\rho v_k \quad \rho v_k v_1 + p\delta_{1k} \quad \rho v_k v_2 + p\delta_{2k} \quad \rho v_k v_3 + p\delta_{3k} \quad \rho v_k h_t]^T$ are the inviscid fluxes. Eq. 1 is solved for the conservative flow variables $\mathbf{U} = [\rho \quad \rho v_1 \quad \rho v_2 \quad \rho v_3 \quad \rho E]^T$ after adding a pseudo-time derivative term. Here, ρ, p, v_k, E, h_t and δ_{km} are the density, pressure, velocity components, total energy per unit mass, total enthalpy and the Kronecker symbol, respectively. Eq. 1 is integrated over the finite volume Ω_P of node P of an unstructured grid, Fig. 1. By applying the Green-Gauss theorem we get

$$\int\limits_{\Omega_P} \left(\frac{\partial f_{nk}}{\partial x_k} \right) d\Omega = \int\limits_{\partial\Omega_P} f_{nk} \hat{\mathsf{n}}_k d\left(\partial\Omega\right) \simeq \sum_{Q \in \mathcal{N}(P)} \Phi_n^{PQ} + \sum_{f \in \mathcal{B}(P)} \Phi_n^f \tag{2}$$

where $\partial\Omega_P$ is the boundary of Ω_P and $\hat{\mathsf{n}}_k$ the unit normal vector pointing outwards. Neighbors $Q \in \mathcal{N}(P)$ and faces $f \in \mathcal{B}(P)$ are defined in Fig. 1. Fluxes Φ_n^{PQ} crossing the

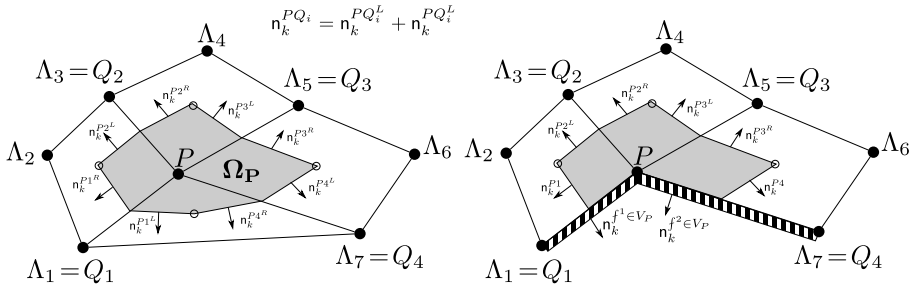

Figure 1: Vertex–centered finite volumes for internal or boundary nodes P of a hybrid $2D$ grid. Nodes Q_i are connected to P via a grid edge, while nodes Λ_i are neighbors of P, connected or not via an edge. $\mathcal{N}(P) = \{\Lambda_i\}, Q_i \in \mathcal{N}(P)$. Similar notation in $3D$.

interface of Ω_P and Ω_Q are discretized using the second-order Roe's upwind scheme,

$$\Phi_n^{PQ} = \frac{1}{2}\left(A_{nmk}^P U_m^P + A_{nmk}^Q U_m^Q \right) \mathsf{n}_k^{PQ} - \frac{1}{2}\left| \tilde{A}_{nmk}^{LR} \mathsf{n}_k^{PQ} \right| \left(U_m^R - U_m^L \right) \tag{3}$$

where $A_{nmk} = \frac{\partial f_{nk}^{\text{inv}}}{\partial U_m}$ is the flux Jacobian and $\tilde{A}_{nmk}$ the Jacobian computed using Roe-averaged quantities, [8]. Superscripts L and R indicate the left (toward P) and right (toward Q) states at this interface and n_k^{PQ} is the dimensional face normal pointing toward Q. U_m^L, U_m^R are computed based on the primitive V_m^L, V_m^R quantities, $\mathbf{V} = [\rho \;\; v_1 \;\; v_2 \;\; v_3 \;\; p]^T$, using Taylor expansions,

$$V_m^L = V_m^P + \frac{1}{2}\mathsf{t}_\ell^{PQ}\frac{\partial V_m^P}{\partial x_\ell}, \qquad \frac{\partial V_m^P}{\partial x_\ell} = D_\ell^P V_m^P + \sum_{\Lambda\in\mathcal{N}(P)} Z_\ell^{P\Lambda} V_m^\Lambda \tag{4a}$$

$$V_m^R = V_m^Q - \frac{1}{2}\mathsf{t}_\ell^{PQ}\frac{\partial V_m^Q}{\partial x_\ell}, \qquad \frac{\partial V_m^Q}{\partial x_\ell} = D_\ell^Q V_m^Q + \sum_{K\in\mathcal{N}(Q)} Z_\ell^{QK} V_m^K \tag{4b}$$

where t_ℓ^{PQ} are the Cartesian components of $\overrightarrow{PQ}$ and D_ℓ, Z_ℓ are geometrical quantities. For the farfield boundary, the Flux Vector Splitting scheme, [9], is used, $\Phi_n^f = A_{nmk}^{+P}\mathsf{n}_k^f U_m^P + A_{nmk}^{-P}\mathsf{n}_k^f U_m^Q$, where Q is a halo node where infinite flow quantities are imposed. Along the solid walls, the no-penetration condition ($v_k\mathsf{n}_k = 0$) yields $\Phi_n^f = \Big[0, p^P\mathsf{n}_k^f,\; 0\Big]$.

3 THE *THINK-DISCRETE-DO-CONTINUOUS* ADJOINT

In continuous adjoint, J is augmented by the field integrals of the product of the state equations' residuals with the adjoint variable fields, $J_{aug} = J + \int_\Omega \Psi_n R_n \mathrm{d}\Omega$. Differentiating J_{aug} w.r.t. the design variables b_i and setting the multipliers of $\frac{\delta U_n}{\delta b_i}$ to zero leads to a new set of PDEs, the so–called field adjoint equations (FAE), and the adjoint boundary conditions (ABC). In an inviscid flow, the FAE are written as, [10].

$$-A_{mnk}\frac{\partial \Psi_m}{\partial x_k} = 0 \tag{5}$$

Its integral over Ω_P is approximated by the following balance of adjoint fluxes

$$-\int_{\Omega_P} A_{mnk}\frac{\partial \Psi_m}{\partial x_k} d\Omega \simeq \sum_Q \Phi_n^{\text{adj},PQ} + \sum_f \Phi_n^{\text{adj},f} \tag{6}$$

A non-conservative discretization scheme for Eq. 6, [1], which mimics the primal one, is

$$\Phi_n^{\text{adj},PQ} = -\frac{1}{2}A_{mnk}^P\mathsf{n}_k^{PQ}\left(\Psi_m^P + \Psi_m^Q\right) - \frac{1}{2}\left|\tilde{A}_{mnk}^{LR}\mathsf{n}_k^{PQ}\right|\left(\Psi_m^R - \Psi_m^L\right) \tag{7}$$

The adjoint solver that makes use of the above discretization scheme will be referred as the standard continuous adjoint. In the *TDDC* adjoint, we seek discretization schemes for $\Phi_n^{\text{adj},PQ}$ and $\Phi_n^{\text{adj},f}$ which are consistent with discrete adjoint and also have a clear physical meaning (as Eq. 7 does). Inspired by discrete adjoint (the presentation of which is beyond the scope of this paper), the following expression for the adjoint fluxes

$$\Phi_n^{\mathbf{adj},PQ,TDDC} = -\frac{1}{2}A_{mnk}^P\mathsf{n}_k^{PQ}\left(\Psi_m^P + \Psi_m^Q\right) - \frac{1}{2}\left[\left(\left|\tilde{\mathcal{A}}_{m\ell k}^{LR}\mathsf{n}_k\right|\Psi_m\right)^{R,\mathbf{adj}} - \left(\left|\tilde{\mathcal{A}}_{m\ell k}^{LR}\mathsf{n}_k\right|\Psi_m\right)^{L,\mathbf{adj}}\right]\frac{\partial V_\ell^P}{\partial U_n^P} \tag{8}$$

is proposed. Here,

$$\phi^{L,\mathrm{adj}}=\phi^P+\frac{1}{2}\left.\frac{\partial\left(\mathsf{t}_r\phi\right)}{\partial x_r}\right|^{P,\mathrm{adj}},\quad \left.\frac{\partial\left(\mathsf{t}_r\phi\right)}{\partial x_r}\right|^{P,\mathrm{adj}}=\mathsf{t}_r^{PQ}D_r^P\phi^P+\sum_{\Lambda\in\mathcal{N}(P)}Z_r^{\Lambda P}\sum_M\mathsf{t}_r^{\Lambda M}\phi^\Lambda \tag{9a}$$

$$\phi^{R,\mathrm{adj}}=\phi^Q+\frac{1}{2}\left.\frac{\partial\left(\mathsf{t}_r\phi\right)}{\partial x_r}\right|^{Q,\mathrm{adj}},\quad \left.\frac{\partial\left(\mathsf{t}_r\phi\right)}{\partial x_r}\right|^{Q,\mathrm{adj}}=\mathsf{t}_r^{PQ}D_r^P\phi^Q+\sum_{\Lambda\in\mathcal{N}(P)}Z_r^{\Lambda P}\sum_M\mathsf{t}_r^{\Lambda M}\phi^M \tag{9b}$$

and M is any node connected to $\Lambda\in\mathcal{N}\left(P\right)$ by an edge. $\left|\tilde{\mathcal{A}}_{m\ell}^{LR}\right|=\left|\tilde{A}_{mn}^{LR}\right|\frac{\partial U_n^L}{\partial V_\ell^L}-\left(U_n^R-U_n^L\right)\frac{\partial\left|\tilde{A}_{mn}^{LR}\right|}{\partial V_\ell^L}$ ($A_{mn}=A_{mnk}\mathsf{n}_k$) is the modified absolute Jacobian which includes the derivatives of the absolute Jacobian w.r.t. the primitive flow variables. This corresponds to an "adjoint" Taylor expansion in the $\mathbf{V}$ space. Note that, if the primal discretization was first-order accurate, an expansion in the $\mathbf{U}$ space would have been used instead.

Apart from the use of the modified absolute Jacobian ($\left|\tilde{\mathcal{A}}_{m\ell}^{LR}\right|$), instead of the standard one (compare Eqs. 7 and 8), the adjoint L and R states ("L,adj", "R,adj") for an adjoint variable are defined differently than in the primal problem. In the primal discretization, Eq. 4, the L state of any variable ϕ, along edge PQ, results from a first-order Taylor expansion and is the sum of ϕ^P and the inner product of the half of $\overrightarrow{PQ}$ and the spatial gradient of ϕ at P. The latter depends on the ϕ values at P and its neighbors Λ_i (Fig. 1). The adjoint L ("L,adj"), Eq. 9, state of ϕ at edge PQ is the sum of the value of ϕ at P and half of the divergence of $\overrightarrow{PQ}$ scaled by ϕ, viz. $\left.\frac{\partial(\mathsf{t}_r\phi)}{\partial x_r}\right|^{P,\mathrm{adj}}$.

Given that this paper is dealing with cases in which J is a force defined in integral form along the walls (airfoil contours or wing surface), in continuous adjoint the wall ABC yields $\Psi_{m+1}\mathsf{n}_m=-\frac{\partial J}{\partial p}$. Since $J=\sum_P p^P\mathsf{n}_k^f r_k$ (r_k is the direction of the component of the force; r_k is different for lift and drag), in discrete sense, $\left.\frac{\partial J}{\partial p}\right|^P=\mathsf{n}_k^f r_k$. Thus, in the *TDDC* adjoint, fluxes crossing the wall boundaries of each finite volume are written as

$$\mathbf{\Phi}^{\mathrm{adj},f,TDDC}=\begin{bmatrix}v_k^P\mathsf{n}_k^f\left[\Psi_{m+1}v_m-\Psi_5\left(-h_t+\frac{\gamma-1}{2}v_kv_k\right)\right]^P\\-\left[\Psi_1+\Psi_{m+1}v_m+\Psi_5h_t\right]^P\mathsf{n}_\lambda^f+v_k^P\mathsf{n}_k^f\left[-\Psi_{\lambda+1}+(\gamma-1)\Psi_5v_\lambda\right]^P\\-\gamma\Psi_5^Pv_k^P\mathsf{n}_k^f\end{bmatrix}+\mathsf{n}_k^fr_k(\gamma-1)\begin{bmatrix}\frac{v_kv_k}{2}\\-v_\lambda\\1\end{bmatrix}^P \tag{10}$$

$\lambda=1,2,3$. The first term in square brackets on the r.h.s. in Eq. 10 refers to the adjoint flux which is independent of J, while the second one is the contribution of J. In the first part, terms $\Psi_{m+1}\mathsf{n}_m$ are absent from the adjoint flux at the wall; this agrees with the ABC in continuous adjoint, if J is not defined along the wall.

In the farfield boundaries, a standard discretization scheme for the adjoint fluxes is $\Phi_n^{\mathrm{adj},f}=-\Psi_m^PA_{mnk}^{-P}\mathsf{n}_k^f-\Psi_m^QA_{mnk}^{-P}\mathsf{n}_k^f$ where, at the halo node, $\Psi_m^Q=0$. In the *TDDC* adjoint, the discretization scheme for the same fluxes becomes

$$\Phi_n^{\mathrm{adj},f,TDDC}=-\Psi_m^P\mathcal{A}_{mnk}^{-P}\mathsf{n}_k^f \tag{11}$$

where $\mathcal{A}^{-P}_{mnk}\mathsf{n}^f_k = \frac{1}{2}\left(A^P_{mnk}\mathsf{n}^f_k - \left|\mathcal{A}^P_{mnk}\mathsf{n}^f_k\right|\right)$ and $\left|\mathcal{A}^P_{mnk}\mathsf{n}^f_k\right| = \left|A^P_{mnk}\mathsf{n}^f_k\right| - \left(U^Q_\ell - U^P_\ell\right)\frac{\partial\left|A^P_{m\ell k}\mathsf{n}^f_k\right|}{\partial U^P_n}$ is the modified absolute Jacobian. Due to the fact that farfield conditions are imposed by means of a single halo node per boundary node, Eq. 11 differs from standard continuous adjoint in the use of the modified absolute Jacobian.

4 SHAPE OPTIMIZATION STUDIES

In the first application, the shape optimization of the isolated NACA0012 airfoil for min. drag coefficient (C_D), with the constraint that the lift coefficient (C_L) remains close to the reference value ($\pm 1‰$) is carried out. An additional inequality constraint, requiring that the airfoil area should not drop below 85% of the starting one, is imposed. The flow is inviscid with $M_\infty = 0.75$ and $\alpha_\infty = 2.0°$. At these conditions, the flow around the starting airfoil is transonic and the presence of a shock wave contributes to the computed drag. The airfoil is parameterized using a 10×7 volumetric NURBS (Non-Uniform Rational B-Splines) control grid, Fig. 3.

The accuracy of the SDs computed using standard continuous and *TDDC* adjoint, on different grids, is investigated; the progressively finer grids consist of $\sim 1.5K$, $\sim 7.8K$ and $\sim 26.4K$ nodes, respectively. C_D and C_L values, as well as their SDs, differ among the three computational grids. The SDs are also compared with Finite Differences (FDs). The computed SDs for C_D and C_L, as well as the optimization convergence histories are illustrated in Fig. 2. In all cases, the *TDDC* adjoint perfectly matches the SDs computed by FDs, even on the coarse, non-adapted to the shock wave, grid. This is why, the three grids compute different transonic flow regions and shocks and, obviously, SDs will be quite different. It is very interesting though that, in all cases, the *TDDC* adjoint computes consistent SDs. The optimization is performed using the sequential least squares programming algorithm (SLSQP), [11]. The SDs based on the *TDDC* adjoint have at least a six significant digit accuracy, even on the coarsest grid. Small discrepancies can be seen with standard continuous adjoint though; these are more intense for the C_D value and, as expected, decrease as grid becomes finer. The difference in the accuracy of SDs affects the optimization; with all grids, the *TDDC* adjoint reduces the C_D value by $\sim 25 - 30\%$, by also meeting the constraints. The Mach number field for the baseline and the optimized (based on the *TDDC* adjoint, on the finest grid that makes sense) airfoil is presented in Fig. 3; the shock strength becomes less strong and this reduces C_D. The baseline and optimized airfoils, as well as the pressure coefficient (C_p) distribution along the airfoil contour, are presented in Fig. 4 for the fine-sized grid.

The shape optimization of an isolated transonic wing for max. lift (L) with the constraint that drag (D) is less or equal to that of the reference wing is, then, studied. The free-stream flow conditions are $M_\infty = 0.8395$, $\alpha_{\infty,\text{pitch}} = 3.06°$ and $\alpha_{\infty,\text{yaw}} = 0°$. The wing shape is controlled by a $8 \times 7 \times 5$ volumetric NURBS control grid, Fig. 5.

The accuracy of the SDs of the two quantities of interest and the optimization convergence history are shown in Fig. 6. The *TDDC* adjoint yields a precision of six significant digits in all SDs; for the standard continuous adjoint small discrepancies in the SDs of D can be seen. The two optimizations lead to $\sim 19.2\%$ and $\sim 21.5\%$ increase in the value of

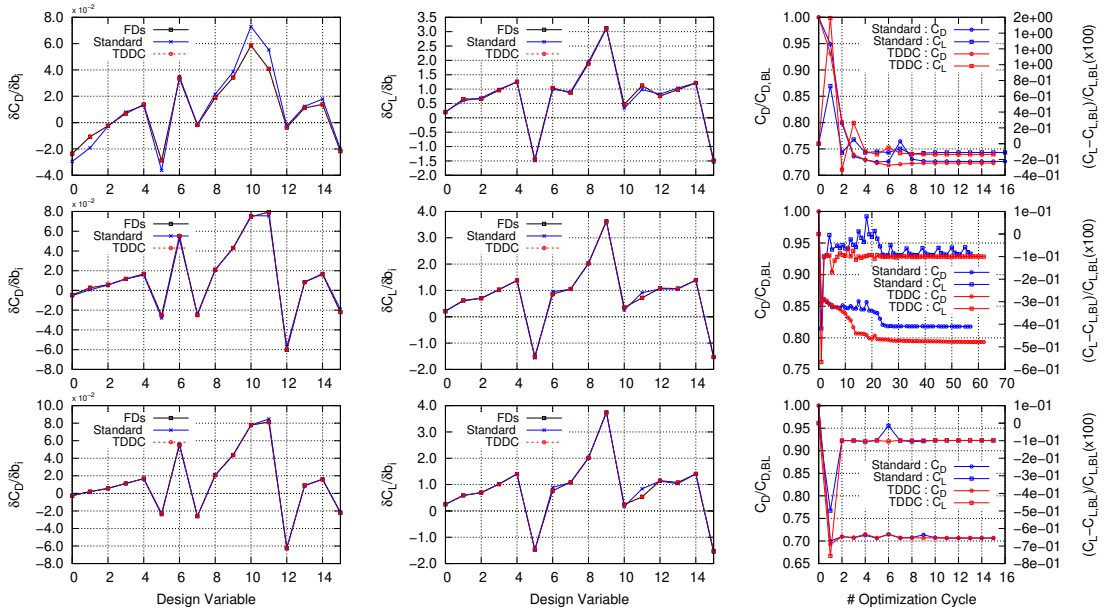

Figure 2: *Isolated Airfoil*: SDs of C_D (left) and C_L (center) computed using FDs, standard continuous and the *TDDC* adjoint on coarse (top), medium (center) and fine (bottom) grids. Evolution of C_D (objective) and C_L (constraint) during the optimization (right).

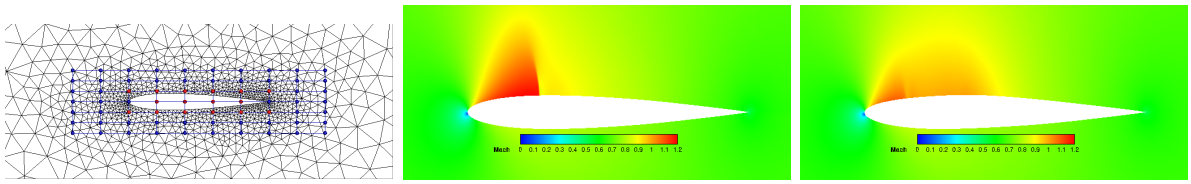

Figure 3: *Isolated Airfoil*: Left: Coarse grid and shape/grid parameterization: control points in blue remain constant, while red ones are allowed to move in the normal-to-the-chord direction, leading to 16 design variables. Mach number fields around the baseline (center) and the optimized (using the *TDDC* adjoint, right) airfoil, on the finest grid.

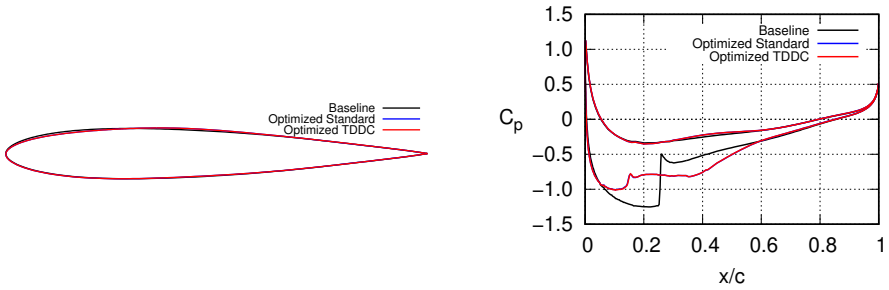

Figure 4: *Isolated Airfoil*: Shape (left) and C_p distribution (right) of the baseline, the optimized airfoils using the standard continuous and the *TDDC* adjoint. On the right, the reduction in pressure recovery (i.e. the reduction in the strength of the shock wave) becomes clear.

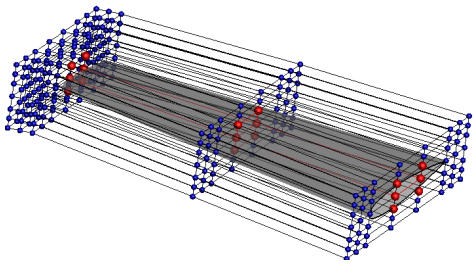

Figure 5: *Transonic Wing*: Parameterization. Control points in blue remain constant, red ones are allowed to move in the chordwise and the normal-to-the-planform directions resulting in 36 design variables.

L, meeting the constraint on D. The flow fields for the baseline and the optimized wings are presented in Fig. 7.

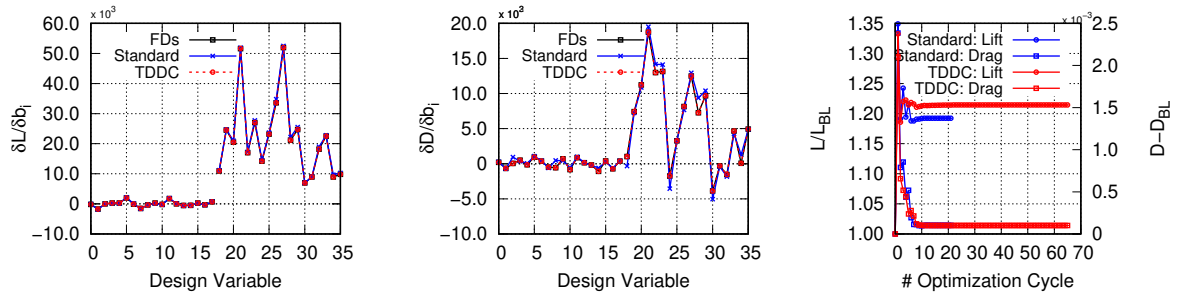

Figure 6: *Transonic Wing*: SDs and optimization history based on the standard continuous and *TDDC* adjoint as well as FDs.

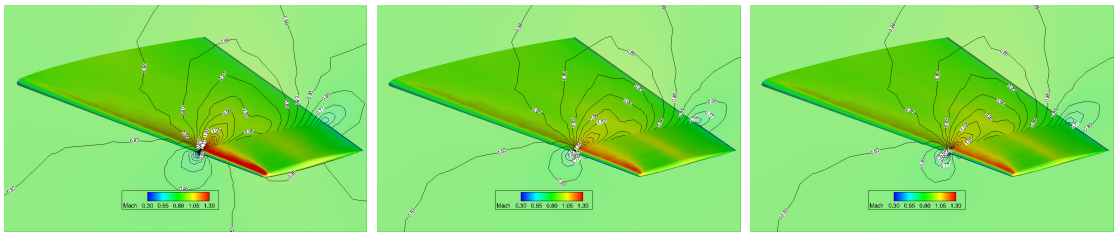

Figure 7: *Transonic Wing*: Mach number field for the baseline (left) and the optimized wing computed using standard continuous (center) and *TDDC* adjoint (right).

5 CONCLUSIONS

The *Think-Discrete-Do-Continuous* (*TDDC*) adjoint presented in this paper reflects research efforts carried out at the Parallel CFD & Optimization Unit of NTUA to create accurate discretization schemes for use in continuous adjoint; to do so, discrete adjoint shows the way. This paper corresponds to the first part of the corresponding research (only for inviscid flows) and the extension to viscous, even turbulent flows (including the adjoint to the turbulence model equations) will follow. The *TDDC* adjoint bridges continuous and discrete adjoint, as it computes exact gradients (this is where discrete adjoint has an advantage) by using interpretable discretization schemes, with minimal

storage requirements (this is where continuous adjoint prevails). This is demonstrated in 2D and 3D applications.

6 ACKNOWLEDGEMENT

This work is supported by the Hellenic Foundation for Research and Innovation (H.F.R.I.) under the "2nd Call for H.F.R.I. Research Projects to support Faculty Members & Researchers" (Project Number: 3821).

REFERENCES

[1] A. Jameson, "Aerodynamic Design via Control Theory". *J. Sci. Comput.*, **3**, 233–260, (1988).

[2] W.K. Anderson, V. Venkatakrishnan, "Aerodynamic design optimization on unstructured grids with a continuous adjoint formulation". *Comput Fluids*, **28**, 443–480, (1999).

[3] J. Elliott, J. Peraire, "Practical three-dimensional aerodynamic design and optimization using unstructured meshes". *AIAA J*, **35**, 1479–1485, (1997).

[4] E.J. Nielsen, W.K. Anderson, "Aerodynamic Design Optimization on Unstructured Meshes Using the Navier-Stokes Equations". *AIAA J*, **37**, 1411–1419, (1999).

[5] M. Giles, M. Duta, J.D. Muller, "Adjoint code developments using the exact discrete approach". *15th AIAA Computational Fluid Dynamics Conference*, Anaheim, CA, USA, June 11–14, (2001).

[6] A. Stuck, T. Rung, "Adjoint complement to viscous finite-volume pressure-correction methods". *J. Comput. Phys.*, **248**, 402–419, (2013).

[7] V.G. Asouti, X.S. Trompoukis, I.C. Kampolis and K.C. Giannakoglou, "Unsteady CFD computations using vertex-centered finite volumes for unstructured grids on GPUs". *Int. J. Numer. Methods Fluids*, **67**, 232–246, (2011).

[8] P. Roe, "Approximate Riemann solvers, parameter vectors, and difference schemes". *J. Comput. Phys.*, **43**, 357–372, (1981).

[9] J.L. Steger, R.F Warming "Flux vector splitting of the inviscid gasdynamic equations with application to finite-difference methods". *J. Comput. Phys.*, **40**, 263–293, (1981).

[10] X.S. Trompoukis, K.T. Tsiakas, V.G. Asouti, K.C. Giannakoglou, "Continuous adjoint-based shape optimization of a turbomachinery stage using a 3D volumetric parameterization". *Int. J. Numer. Methods Fluids*, (to appear, 2023).

[11] J. Nocedal, S.J. Wright, "Numerical Optimization". Springer, NY, USA, (2001).